Particle-in-cell simulations of the solar wind interaction with lunar crustal magnetic anomalies: Magnetic cusp regions

A. R. Poppe,[1,2] J. S. Halekas,[1,2] G. T. Delory,[1,2] and W. M. Farrell[2,3]

[1] As the solar wind is incident upon the lunar surface, it will occasionally encounter lunar crustal remanent magnetic fields. These magnetic fields are small-scale, highly non-dipolar, have strengths up to hundreds of nanotesla, and typically interact with the solar wind in a kinetic fashion. Simulations, theoretical analyses, and spacecraft observations have shown that crustal fields can reflect solar wind protons via a combination of magnetic and electrostatic reflection; however, analyses of surface properties have suggested that protons may still access the lunar surface in the cusp regions of crustal magnetic fields. In this first report from a planned series of studies, we use a $1^{1}/_{2}$-dimensional, electrostatic particle-in-cell code to model the self-consistent interaction between the solar wind, the cusp regions of lunar crustal remanent magnetic fields, and the lunar surface. We describe the self-consistent electrostatic environment within crustal cusp regions and discuss the implications of this work for the role that crustal fields may play regulating space weathering of the lunar surface via proton bombardment.

Citation: Poppe, A. R., J. S. Halekas, G. T. Delory, and W. M. Farrell (2012), Particle-in-cell simulations of the solar wind interaction with lunar crustal magnetic anomalies: Magnetic cusp regions, *J. Geophys. Res.*, *117*, A09105, doi:10.1029/2012JA017844.

1. Introduction

1.1. Lunar Crustal Magnetic Fields

[2] A vast majority of bodies in the solar system are immersed in the supersonic flow of the solar wind and the interaction of each body with the solar wind can be classified according to the strength of the body's intrinsic magnetic field. Objects with a dipolar and relatively strong magnetic field (Earth, Jupiter, Saturn, etc.) are shielded from direct contact as the solar wind is diverted around the body's magnetosphere. In contrast, bodies with weaker (Mercury), non-dipolar or incoherent (the Moon, Mars), or no intrinsic magnetic field (Venus), have portions of their atmospheres or surfaces directly exposed to the solar wind. This exposure leads to diverse physical processes, including atmospheric loss, electrostatic surface charging, sputtering of surface constituents, and the formation of wake structures downstream from the body.

[3] Crustal remanent magnetic fields on the Moon were quickly recognized from surface and orbital spacecraft magnetometer measurements and from analysis of remanent magnetization in lunar samples during the Apollo era [*Dyal et al.*, 1970, 1974; *Sharp et al.*, 1973; *Russell et al.*, 1973; *Fuller*, 1974]. Additional, higher-resolution in-situ measurements were made by the Lunar Prospector Magnetometer and Electrostatic Analyzer [*Lin et al.*, 1998; *Halekas et al.*, 2001], and have facilitated the calculation of global maps of the magnetic field strength at spacecraft altitudes ($\approx$30 km) and at the lunar surface [*Hood et al.*, 2001; *Mitchell et al.*, 2008; *Richmond and Hood*, 2008; *Purucker*, 2008; *Purucker and Nicholas*, 2010]. These magnetic fields are non-dipolar, of relatively small spatial extent (compared to the lunar radius), and mainly clustered on the far side of the Moon. The origin of these fields is not entirely clear, with various theories suggesting the presence of an early lunar dynamo [*Garrick-Bethell et al.*, 2009; *Hood*, 2011] or shock magnetization from meteoroid impacts [*Hood and Huang*, 1991; *Halekas et al.*, 2003; *Hood and Artemieva*, 2008].

[4] Several spacecraft have observed the interaction between lunar crustal magnetic fields and the solar wind, including Explorer 35, Lunar Prospector, Chandraya'an-1, Kaguya, and most recently, the Acceleration, Reconnection, Turbulence, and Electrodynamics of the Moon's Interaction with the Sun (ARTEMIS) mission [*Angelopoulos*, 2010; *Sibeck et al.*, 2011]. These observations have revealed a wealth of electromagnetic phenomena, including limb shocks [*Russell and Lichtenstein*, 1975; *Lin et al.*, 1998; *Halekas et al.*, 2006b, 2008a], whistler and electrostatic solitary waves [*Halekas et al.*, 2006a; *Hashimoto et al.*, 2010], broadband electrostatic noise [*Halekas et al.*, 2008a], reflection of up to 50% of the incident solar wind [*Lue et al.*, 2011], and the presence of steady state electrostatic potentials above lunar crustal magnetic anomalies [*Saito et al.*, 2012]. The small spatial scale of lunar crustal anomalies relative to

[1]Space Sciences Laboratory, University of California, Berkeley, California, USA.
[2]NASA Lunar Science Institute, Ames Research Center, Mountain View, California, USA.
[3]NASA Goddard Space Flight Center, Greenbelt, Maryland, USA.

Corresponding author: A. R. Poppe, Space Sciences Laboratory, University of California, 7 Gauss Way, Berkeley, CA 94720, USA. (poppe@ssl.berkeley.edu)

both the lunar radius and a typical solar wind proton gyro-radius is typically thought to imply that coherent, shock-like structures cannot form above magnetic anomalies; however, simulations and observational evidence have suggested that in some cases, lunar crustal fields may be strong enough to stand off the solar wind and form a mini-magnetosphere [*Harnett and Winglee*, 2000, 2002, 2003; *Kurata et al.*, 2005; *Halekas et al.*, 2008b; *Wieser et al.*, 2010; *Lue et al.*, 2011]. For crustal magnetic anomalies that are either weaker or smaller in scale, the interaction with the solar wind transitions into a more kinetic regime. In these cases, solar wind protons have gyroradii larger than the magnetic anomaly scale size, implying a highly non-adiabatic interaction. Indeed, a wide range of interaction modes most likely exists between the solar wind and lunar crustal magnetic fields, depending on the scale size, strength, and topology of the fields, and these modes have yet to be thoroughly observed, catalogued, and analyzed.

[5] The presence of the lunar surface, which will electro-statically charge in response to ambient and photoemissive currents [*Freeman and Ibrahim*, 1975; *Halekas et al.*, 2008c], may also influence the interaction of the solar wind with lunar crustal magnetic anomalies. The plasma environment within approximately twenty-five meters of the dayside lunar surface is typically dominated by the presence of a photoelectron sheath, a non-neutral charge layer of photo-emitted electrons [*Poppe and Horányi*, 2010]. In cases without photoemission, the lunar surface typically charges negative due to the higher mobility of solar wind electrons [*Halekas et al.*, 2002, 2005]. In either case, the electrostatic surface charge is expected to dominate the near-surface lunar plasma environment; however, the effect of the simultaneous presence of the charged lunar surface and a crustal anomaly on the plasma environment near the Moon has not yet been fully explored.

1.2. Lunar Swirls and Surface Hydroxyl Signatures

[6] The presence of sinuous, high-albedo patterns on the lunar surface, known as lunar swirls, has long been a subject of interest since their discovery during the Apollo era [*El-Baz*, 1972]. Lunar swirls appear on both highland and mare terrains, appear to be completely surficial in nature, and have a high degree of correlation with the presence of remanent lunar crustal magnetic anomalies [*Hood and Williams*, 1989; *Richmond et al.*, 2003; *Neish et al.*, 2011]. Several theories have been proposed regarding the formation of swirls, including the deposition of high-albedo coma material (gas and/or dust) onto the lunar surface from recent cometary impacts [*Schultz and Srnka*, 1980], differential space weathering caused by shielding of the lunar surface from solar wind bombardment by lunar crustal remanent magnetic fields [*Hood and Schubert*, 1980; *Hood and Williams*, 1989], and differential transport of high-albedo lunar dust grains into magnetically shielded regions [*Garrick-Bethell et al.*, 2011]. While the cometary impact theory maintains that lunar swirls and crustal remanent magnetic fields are both generated as a result of a cometary impact (in order to explain the correlation between the two), both the solar wind standoff and lunar dust grain transport theories maintain that crustal remanent magnetic fields, whatever their source may be, are the cause of lunar swirls (albeit via different mechanisms), rather than a simultaneous effect of another process.

[7] The solar wind shielding model for the formation of lunar swirls postulates that swirls form on the lunar surface in areas where crustal remanent magnetic fields either partially or completely inhibit the influx of solar wind or terrestrial magnetospheric protons. In addition to micrometeorite bombardment, high-energy protons are a known agent of space weathering, the process by which external factors cause regolith to undergo spectral and compositional changes, including a general decrease of the regolith's reflectance and the production of nanophase iron ($npFe^0$) on and within lunar regolith grains [*Pieters et al.*, 1993; *Hapke*, 2001; *Noble et al.*, 2007; *Kramer et al.*, 2011a, 2011b]. If crustal remanent fields can shield and/or reflect significant enough amounts of incoming protons, the regolith beneath such fields will experience a lesser rate of space weathering, and in turn, have brighter reflectances relative to magnetically unprotected regions, thus producing the observed lunar swirls [*Hood and Schubert*, 1980; *Hood and Williams*, 1989]. A variety of simulations have shown that a collection of sub-surface dipoles with fields resembling that of lunar crustal anomalies can deflect solar wind protons from bombarding the surface, while focusing ions into other regions [*Hood and Williams*, 1989; *Harnett and Winglee*, 2000, 2002, 2003], lending support to the solar wind shielding model. Recent analysis and experimental work has provided further evidence for this model by showing the development of a thin electrostatic layer immediately above a simulated magnetic anomaly that can serve to electrostatically repel the incoming solar wind protons [*Bamford et al.*, 2012].

[8] Additional evidence for solar wind shielding of the lunar surface by crustal magnetic anomalies has come from a recent analysis of spectroscopic observations of the lunar regolith. Following the discovery of spectroscopic signatures of either hydroxyl or water on the surface of the Moon [*Pieters et al.*, 2009; *Sunshine et al.*, 2009; *Clark*, 2009], regions with lunar swirls were shown to be deficient in surficial hydroxyl relative to unshielded regions [*Kramer et al.*, 2011b]. The main hypothesis regarding the production of hydroxyl in lunar regolith is via the implantation of solar wind protons as they bombard the surface and bond with oxygen [*Pieters et al.*, 2009; *Managadze et al.*, 2011]. Correspondingly, areas shielded from the solar wind by crustal magnetic anomalies should bear less hydroxyl, which is indeed what is observed.

[9] While lunar swirls are mainly characterized by the presence of high-albedo regions, an equally important feature is the presence of 'dark lanes'. Dark lanes are narrow regions of distinctly low albedo regolith immediately adjacent to regions of high albedo, resulting in a striking visual contrast [*Bell and Hawke*, 1982; *Pinet et al.*, 2000; *Blewett et al.*, 2007]. Dark lanes are thought to be regions of the surface under areas of open magnetic access, into which solar wind protons can still penetrate and effectively weather. Recent work has shown that dark lines identified via optical images have strong spectroscopic signatures of hydroxyl, similar to magnetically unshielded areas [*Kramer et al.*, 2011a]. Early particle-tracing simulations found that simple models of crustal magnetic anomalies could produce regions of the surface that suffered a greater rate of solar wind proton bombardment via deflection of incoming proton trajectories than adjacent magnetically shielded regions [*Hood and Williams*, 1989]; however, this type of modeling

does not account for self-consistent electrostatic plasma effects, which could feedback on the incident solar wind.

[10] In summary, the various analyses and models presented in favor of the solar wind shielding hypothesis present a qualitatively coherent picture for a formation mechanism for lunar swirls. In order to further our understanding of the role of crustal magnetic anomalies in the evolution and weathering of the lunar surface, it is necessary to move toward a more quantitative approach. Using a series of increasingly sophisticated particle-in-cell simulations, we aim to determine, among other quantities, the electrostatic potential as a function of height within anomalies, the effect that this potential has on the incoming particle distributions, and the proton number and energy flux to the lunar surface as a function of crustal magnetic field strength. We can then compare this information to in-situ measurements at the Moon of electrostatic potentials within crustal magnetic anomalies to further constrain the solar wind shielding hypothesis. Our first investigation, presented here, uses a $1\frac{1}{2}$-dimensional particle-in-cell simulation to model the electrostatic environment specifically within the cusp regions of lunar crustal magnetic anomalies. In Section 2, we describe the technical details of the simulation code and present results for a variety of crustal magnetic field strengths. In Section 3, we discuss the results of the simulations and outline how these results impact the phenomena presented in Section 1.2. Finally, we conclude and identify future work in Section 4.

2. Simulations

2.1. Model Description

[11] In order to simulate the interaction of the solar wind with crustal remanent magnetic field cusps, we use a $1\frac{1}{2}$-dimensional, electrostatic particle-in-cell (PIC) code, modified from a 1-dimensional PIC code previously used to model the dayside lunar plasma environment [*Birdsall and Langdon*, 1985; *Poppe and Horányi*, 2010; *Poppe et al.*, 2011, 2012]. The $1\frac{1}{2}$-d code is identical to the 1-d code, with the addition that a static magnetic field is present and perpendicular velocities are tracked for electrons. While an in-depth description of the 1-d code can be found in *Poppe and Horanyi* [2010], we briefly describe its main features here. The model simulates the direction normal to the Moon, with the left end representing the lunar surface and the right end representing the ambient plasma environment. Closed boundary conditions are used at the lunar surface by continuously keeping track of absorbed and emitted particles and from there, calculating the lunar surface charge. Open boundary conditions are used at the other end, where the solar wind is injected. Using the positions of the particles, the charge density, electric potential (via Poisson's equation), and electric field are calculated. Particles are advanced at each step by calculating both the electric force and any magnetic mirroring force (discussed further in the next paragraph). The process is continuously repeated in order to advance the simulation in time. The solar wind is injected from the upper end of the simulation, with a density of approximately, $n_{sw} = 5 \times 10^6$ m^{-3}, ion and electron temperatures, $kT_i = kT_e = 10$ eV, and a bulk drift speed of 450 km/sec. The ion-electron mass ratio was set to 800, which corresponds to a proton Mach number of $M = 9.6$. This ion-electron mass ratio was selected in order to obtain a

supersonic proton beam without rendering the proton dynamics computationally prohibitive. An analysis of the dependence of our results on the ion-electron mass ratio is presented in Section 2.2.1. The simulation length was set to 30 km and used a spatially varying grid size ranging from approximately 25 m far from the lunar surface to less than 1 m near the surface in order to provide resolution at or below the Debye length throughout the simulation. At least 40,000 particles of each species are tracked throughout the simulation, providing sufficient particle statistics in the model. In order to understand the separate contributions of the solar wind and lunar photoelectrons to the equilibrium electrostatic solution, the simulations presented here are without the presence of photoemission. At periodic intervals, the simulation reports out the positions and velocities of each species (from which the density can be obtained), the electric potential, the electric field, and the lunar surface charge. The simulation is first allowed to come to equilibrium before using any reported data for analysis.

[12] The $1\frac{1}{2}$-d PIC code by nature cannot explicitly model the full, three-dimensional, non-adiabatic ion interaction that is present within lunar crustal magnetic anomalies. Therefore, we instead investigate a simplified situation in which the incoming solar wind encounters the open cusp region of a small-scale magnetic anomaly with the solar wind velocity vector directly normal to the surface, down the axis of the magnetic cusp. The scale of the anomaly (discussed later in this section) is set such that the adiabatic invariant of the solar wind electrons is conserved, while the solar wind protons can be considered unmagnetized in the lunar frame. In this case, the electrons respond self-consistently to both the electrostatic field and the cusp magnetic field (as described using the adiabatic invariant) while the solar wind protons are only affected by the electrostatic field. As a $1\frac{1}{2}$-d PIC code, the model cannot describe field and particle variations in the lateral dimensions (parallel to the lunar surface) which are important in understanding the ability of crustal magnetic anomalies to shield the lunar surface [*Harnett and Winglee*, 2003; *Wang et al.*, 2012]. Higher-dimensional PIC simulations of the solar wind interaction with lunar crustal magnetic anomalies can address these lateral variations, and we aim to lay the groundwork for these higher-dimensional simulations by first considering the simplified model presented here.

[13] The magnetic field in the simulation, $B(z)$, is comprised of two components: the background interplanetary magnetic field, $B_{sw} = 10$ nT, constant in time and space in all simulations, and the crustal anomaly field, $B_a(z)$, which varies along the simulation axis, but is also constant in time. Similar to previous work, we model the crustal anomaly field as a magnetic dipole with moment, m_o, buried at some depth, h, below the lunar surface [*Hood and Williams*, 1989], oriented such that the dipole is aligned with the simulation axis, representative of the cusp regions of crustal magnetic anomalies. The strength of the anomaly magnetic field then has the form, $B_a(z) \propto 1/(z + h)^3$, with derivative $dB_a(z)/dz \propto 1/(z + h)^4$, which generates the magnetic mirror restoring force,

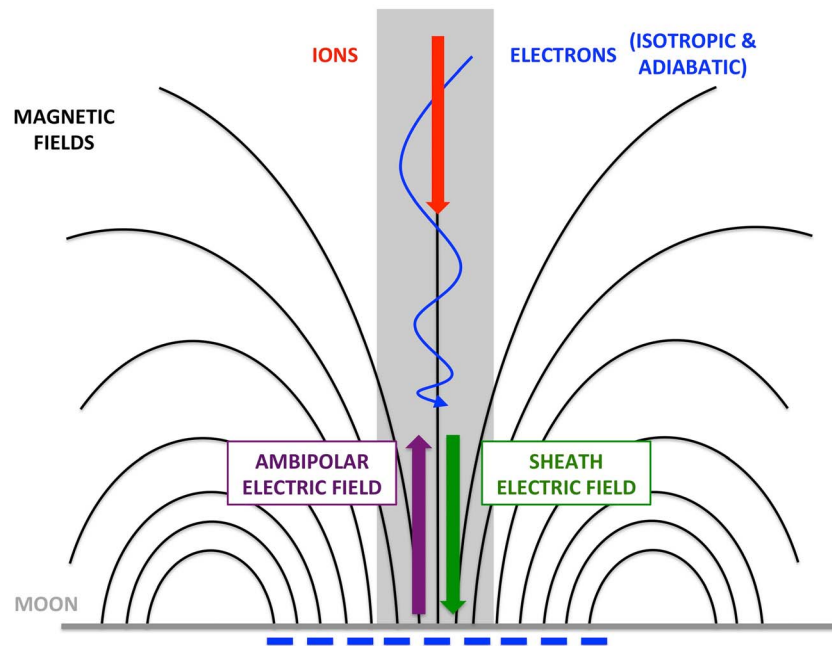$$F(z) = -\mu \frac{dB_a(z)}{dz}, \qquad (1)$$

Figure 1. A cartoon illustrating the geometry and various particle populations and fields present in the model as explained in the text.

where $\mu = \frac{1}{2}mv_{\perp}^2/B$ is the magnetic moment of an electron. As solar wind electrons enter the simulation, they are assigned parallel and perpendicular velocities with the desired distributions. Using the initial perpendicular velocity and the local value of the magnetic field, the magnetic moment for each electron can be calculated. The adiabatic assumption states that $d\mu/dt = 0$, and thus, we can use the conservation of μ to calculate the perpendicular velocity at any later point in time by using the strength of the magnetic field at the electron's location. Parallel electron velocities, $v_{\parallel}(z)$, are subject to the sum of the electrostatic and magnetic mirror forces,

$$m\frac{dv_{\parallel}(z)}{dt} = -q\nabla\phi(z) - \mu\frac{dB(z)}{dz}, \qquad (2)$$

where m is the electron mass, q is the electron charge, and $\phi(z)$ is the electrostatic potential. It is important to note that while the electric force depends on the charge of the particle, the magnetic mirror force does not, and for the magnetic field model used here, always points away from the surface for electrons.

[14] Figure 1 is a cartoon overview of the various particle populations and fields present in the model. Shown in dark grey and black, respectively, are the lunar surface and a dipolar model of the lunar crustal remanent magnetic field. The simulation axis models the central field line, normal to the lunar surface, as discussed above, and shaded in light gray in Figure 1. Solar wind electrons (blue) and ions (red) enter the magnetic anomaly region, with electrons gyrating around the magnetic field lines while ions penetrate directly into the anomaly region. The electrons are fully adiabatic ($d\mu/dt = 0$) and isotropic ($T_{e,\parallel} = T_{e,\perp}$). In the absence of photoemission, the lunar surface will typically charge negative, with an accompanying sheath electric field pointing

into the surface (green). Opposing this field is an ambipolar electric field (purple) generated due to a differential charge separation as electrons and ions penetrate the crustal magnetic anomaly to different typical heights above the lunar surface. Previous theoretical work has shown that in a pure magnetic mirror (i.e. no surface present) the ambipolar electric field is zero if and only if the electron and ion pitch angle distributions are identical [*Persson*, 1963, 1966]. For the solar wind, this condition is certainly not satisfied, as the solar wind flow speed implies that the ions are a supersonic beam (in the lunar frame), while the electrons are an isotropic, thermalized background. Thus, when combining the interaction of the solar wind with both the lunar surface and the crustal magnetic anomaly cusp, we expect to find both downward-pointing sheath electric fields and upward-pointing ambipolar electric fields; however, these fields do not necessarily have identical strengths as a function of height above the lunar surface and thus, we cannot *a priori* predict the self-consistent equilibrium solution when these phenomena are combined. Based on observations discussed in Section 1.2, we expect a significant solar wind flux to penetrate any electrostatic potentials in the cusp region of the anomaly and impact the lunar surface; however, the role of the electrostatic potential in regulating this flux is not yet well understood.

[15] For the magnetic field, we set a constant dipole depth below the lunar surface of $h = 2.5$ km and vary the magnetic moment magnitude in order to set the crustal magnetic field strength at the surface to a discrete set of values ranging from 1 nT to 10,000 nT. Figure 2 shows a log-log plot of the total magnetic field strength (crustal plus background solar wind) as a function of height above the lunar surface for the range of simulated surface crustal field strengths. In all cases, the dipole field is essentially constant below 100 m, and transitions from the maximum value to the background
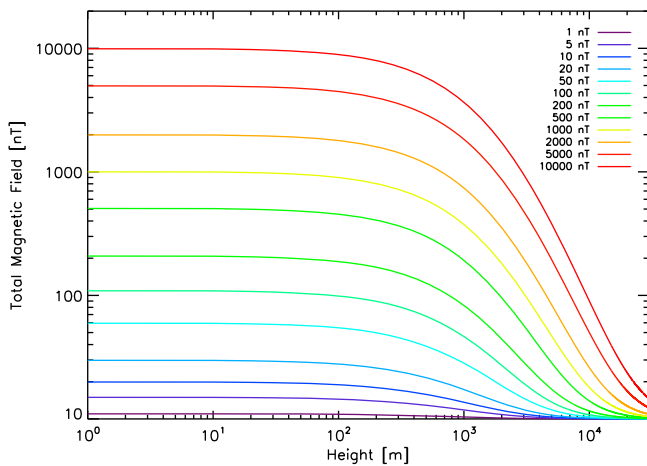
Figure 2. The total magnetic field strength (crustal plus solar wind) as a function of height above the lunar surface for the various crustal field strengths modeled.

value of 10 nT between 100 m and 30 km. For the highest crustal field strengths, the total field does not completely return to the background solar wind value by the time the simulation boundary has been reached; however, the 'excess' crustal field strength at the boundary is less than 0.1% of the maximum crustal field strength and thus, represents a minor approximation. Throughout the discussion, individual runs with a specific crustal field strength are identified by the maximum crustal field strength at the surface (i.e., '10 nT' refers to the case of a 10 nT maximum crustal field at the surface, which is in turn added to the 10 nT background magnetic field, for a total field strength of 20 nT at the surface). The anomaly scale used here can be compared against both the electron and proton gyroradii to ensure that the assumption of magnetized electrons and unmagnetized ions is preserved. For the electrons, the typical gyroradius, $r_{L,e}$, in the solar wind is approximately 1 km, somewhat smaller than the crustal field scale length of $h = 2.5$ km. As the solar wind electrons enter the crustal anomaly region and the field strength increases, the gyro radius correspondingly decreases and $r_{L,e}/h \ll 1$ throughout the simulation domain. On the other hand, the solar wind proton drift gyroradius, $r_{L,i}$ (which, rather than the thermal gyroradius, is the appropriate scale to consider as the solar wind impinges on the anomaly), is approximately 400 km for a 10 nT crustal field, implying that $r_{L,i}/h \gg 1$. As the crustal field strength increases, this ratio will decrease; however, only for the strongest fields ($B > 1000$ nT) will this ratio approach unity. Therefore, the assumption of magnetized electrons and unmagnetized ions holds for the geometry and field strengths considered in this model.

[16] We note here that while we have simulated maximum crustal field strengths up to 10,000 nT, we do not necessarily believe that such large magnetic fields exist at the lunar surface. Rather, we have done so in order to examine properties of the interaction of the solar wind with crustal magnetic anomalies over a parameter range sufficiently wide enough to discern trends and draw conclusions therefrom. The question of the maximum crustal field strength at the lunar surface is in fact presently open, with the largest-known measured value to date coming from the Apollo 16

surface magnetometer measurements [*Dyal et al.*, 1974]. The magnetometer recorded a value of 327 nT in the vicinity of the Descartes anomaly, one of the strongest concentrations of magnetic fields on the lunar nearside [*Halekas et al.*, 2001]. Additionally, the Lunar Prospector Electron Reflectometer has inferred crustal field strengths at the lunar surface of hundreds of nT [*Lin et al.*, 1998; *Halekas et al.*, 2001], and a recent re-analysis of the electron reflectometry (ER) technique has suggested that in cases where the spatial wavelength of the magnetization is sub-kilometer scale in nature or the magnetization is highly spatially incoherent, that ER may underestimate the surface magnetic field strength, implying field strengths upwards of 1000 nT [*Halekas et al.*, 2010]. Nevertheless, in the absence of direct knowledge of the maximum surface crustal magnetic field strength, we feel that values between 1 and 10,000 nT represent a suitable range for our studies.

2.2. Model Results

2.2.1. Electrostatic Potentials

[17] Figure 3a shows the modeled equilibrium electrostatic potential as a function of height above the lunar surface for all crustal magnetic field strengths. The potentials for low crustal field strengths (<20 nT) at the surface are slightly negative (≈ -10 V) with respect to infinity, which is expected for typical, non-photoemissive solar wind plasma sheaths, in which the lighter electrons charge the surface at a higher rate than ions and an equilibrium is established with a negative surface charge and a positive space charge above the surface for the first few tens of meters [*Whipple*, 1981; *Chen*, 1984]. For field strengths greater than 20 nT, the electrostatic potential begins to shift upward, with a maximum occurring at approximately 150 m above the lunar surface. Above this height, the potential slopes downward toward infinity, creating an upward-pointing electric field that slows incident ions and accelerates incident electrons. Below approximately 150 m, the slope of the potential, and thus, the sign of the electric field, is reversed, with a plasma sheath electric field pointing inward to a negatively charged lunar surface. The potential below 150 m will serve to re-accelerate any solar wind ions that have penetrated the maximum electrostatic potential into the surface. As a comparison, typical sheath electrostatic potentials on the lunar dayside in the solar wind in magnetically unshielded regions have magnitudes of approximately 5–10 V [*Halekas et al.*, 2008c; *Poppe and Horányi*, 2010; *Halekas et al.*, 2012], and thus, electrostatic potentials generated from solar wind interactions with crustal magnetic fields should dominate, at least at high altitudes.

[18] Another way to characterize the strength of the magnetically induced electrostatic potential is to examine the ratio of the maximum electrostatic potential energy with respect to infinity to the bulk energy of the incident solar wind protons, $E_{sw} = 0.5 m_i^* v_{sw}^2$, where $m_i^* = 800 m_e$ is the simulation ion mass and $v_{sw} = 450$ km/sec is the bulk solar wind speed. We show this ratio in Figure 3b. As the crustal field strength increases, this ratio increases correspondingly, and reaches unity at the strongest fields considered here ($B_a = 10,000$ nT). Electrostatic potential energies at or in excess of the solar wind bulk energy are possible given that the solar wind proton beam is not mono-energetic at the drift energy, but rather contains a finite thermal spread in addition
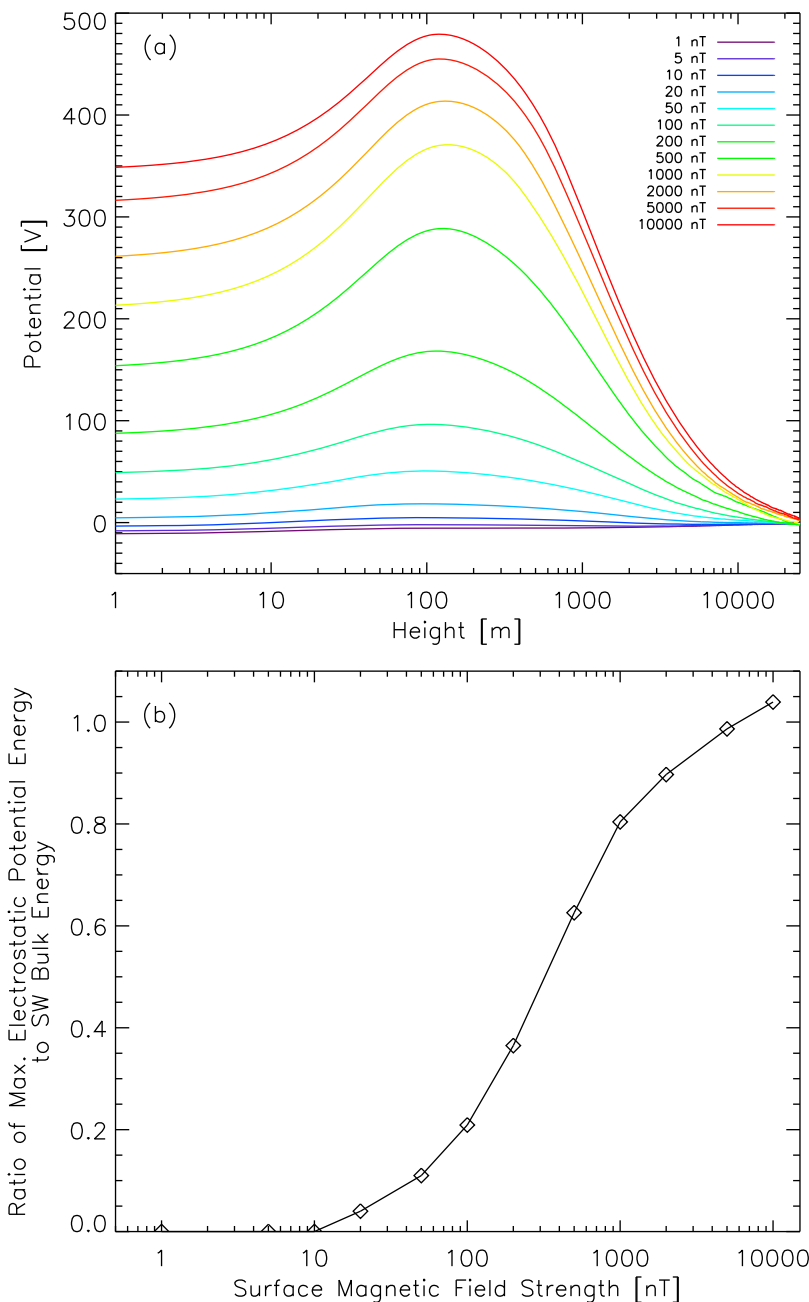
Figure 3. (a) The potential as a function of height above the lunar surface for varying values of the surface crustal magnetic field strength. (b) The ratio of the maximum electrostatic potential energy to the incident solar wind proton bulk energy as a function of crustal magnetic field strength.

to the drift energy. While we have presented this ratio for an ion/electron mass ratio of 800, we have run a subset of simulations at ion/electron mass ratios of 400 and 1200 in order to ascertain the dependence of the electrostatic potential energy on the incoming ion mass. In Figure 4, the ratio of the maximum electrostatic energy to the incoming solar wind bulk energy decreases slightly for increasing ion/electron mass ratios; however, an extrapolation out to the physical ion/electron mass ratio ($m_i/m_e = 1836$) would still indicate significant electrostatic potential strengths. We compare these modeled potentials to those measured by the KAGUYA

spacecraft within crustal magnetic anomalies in Section 3 [*Saito et al.*, 2012].

2.2.2. Ion Distributions

[19] To investigate the effect that the electrostatic potentials have on the incoming solar wind protons, we analyze the proton velocity distribution at different heights above the lunar surface. Figure 5 shows the normalized parallel velocity distributions for solar wind protons at two heights above the lunar surface: 20 km and 0.1 km, with negative velocities corresponding to ions moving toward the Moon. In Figure 5a, the incident ion distribution ($v_∥ < 0$) at 20 km shows no obvious modification over all crustal field
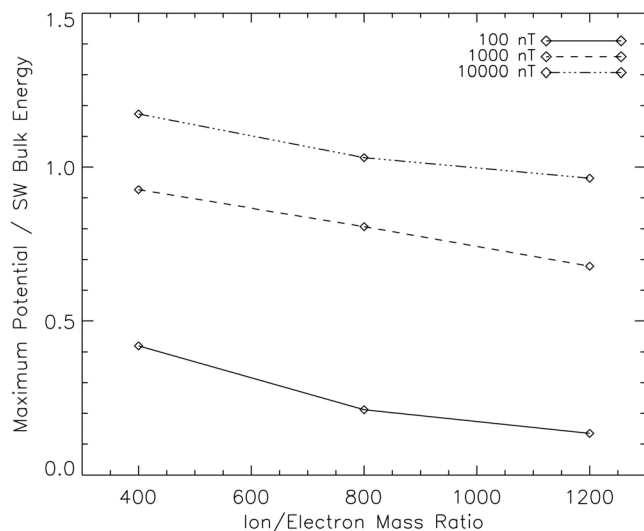
Figure 4. The maximum ratio of electrostatic potential to incident solar wind bulk energy as a function of the simulation ion/electron mass ratio for three different magnetic field strengths (100, 1000, 10000 nT).

strengths modeled. For large enough crustal field strengths ($> 100 - 200$ nT), a reflected ion population ($v_{\parallel} > 0$) appears, consisting of incident solar wind protons with energies too low to overcome the magnetic anomaly induced electrostatic potential. The resulting ion distribution at 20 km consists of two supersonic, anti-parallel proton beams, which, as will be shown and discussed later, induces an ion-ion two stream instability, with corresponding ion phase space holes and ion heating.

[20] At a distance of only 0.1 km above the lunar surface, deep within the crustal anomaly field, the ion distribution shows considerable modification that is highly dependent on the crustal field strength (Figure 5b). As the field strength increases, the ions at 0.1 km are both decelerated in bulk and heated. The deceleration is due to the presence of the electrostatic potential while the heating is due to the presence of an ion-ion two-stream instability. For the higher crustal field values (>200 nT), the low-energy tail of the incident ion Maxwellian is mainly missing, having been electrostatically reflected before reaching 0.1 km. Importantly, the ion distribution at 0.1 km will be re-accelerated into the lunar surface by the sheath field, which points inward to the surface due to the accumulation of negative surface charge.

2.2.3. Ion Distribution Moments

[21] The effect of the magnetic and electrostatic fields on the solar wind proton distributions can also be analyzed by calculating the moments of the distributions, namely, the density, bulk speed, and temperature. Figure 6 shows these values as a function of height above the lunar surface for both incident and reflected protons, normalized to the respective incident value for 1 nT crustal magnetic field at 25 km height. The colors correspond to magnetic field strengths at the surface, using the same legend as earlier plots. For heights above which the ion distribution can be separated into two distinct distributions ($z > 750$ m), we present separate velocity and temperature moments for incident and reflected ions, respectively. For heights below this, the incident velocity and

temperature are calculated over the entire distribution and shaded grey regions denote moments for the reflected population that are not valid.

[22] For the ion densities, shown in Figures 6a and 6b, one easily sees that for low crustal field strengths, there is little effect on the incident solar wind. Specifically, for field strengths less than approximately 100 nT, there is no reflected population and only a slight increase in the density of the incident population as the electrostatic potential decelerates the solar wind ions. As field strengths surpass 100 nT, the incident and reflected densities continue to increase near the surface, as an increasing fraction of the incident protons are
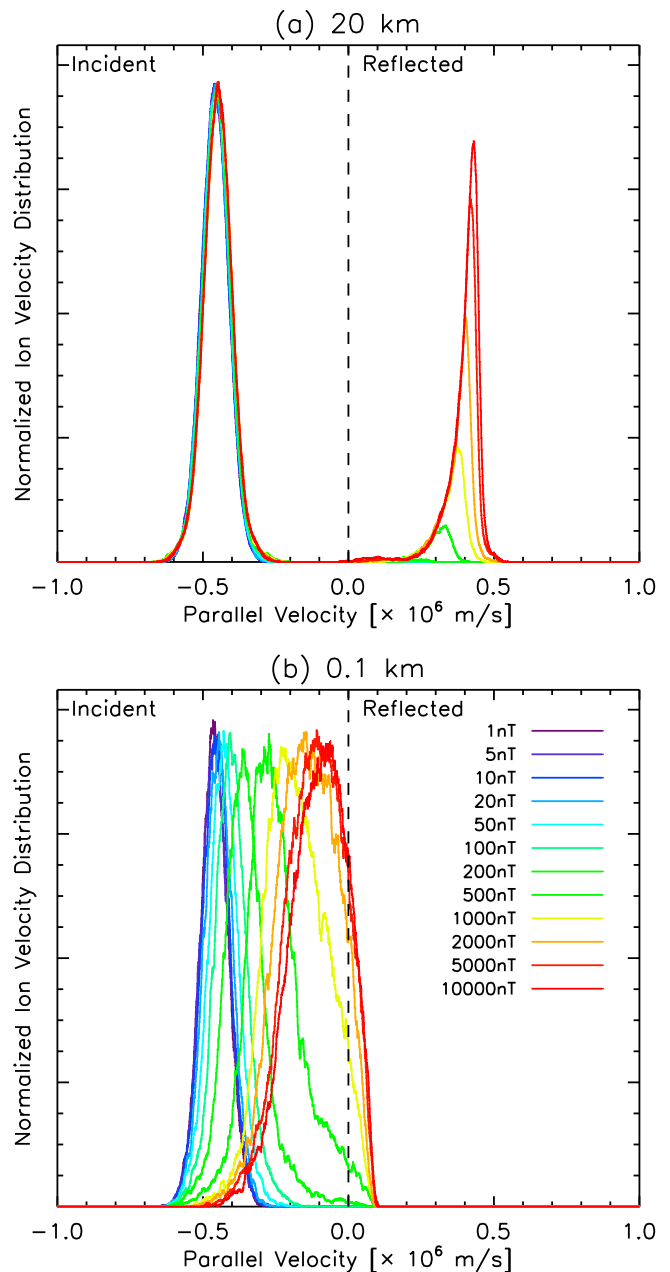

Figure 5. The ion parallel velocity distribution for all cases of the modeled magnetic field, at two different heights above the lunar surface, (a) 20 km and (b) 0.1 km. The color legend is identical to that used earlier.
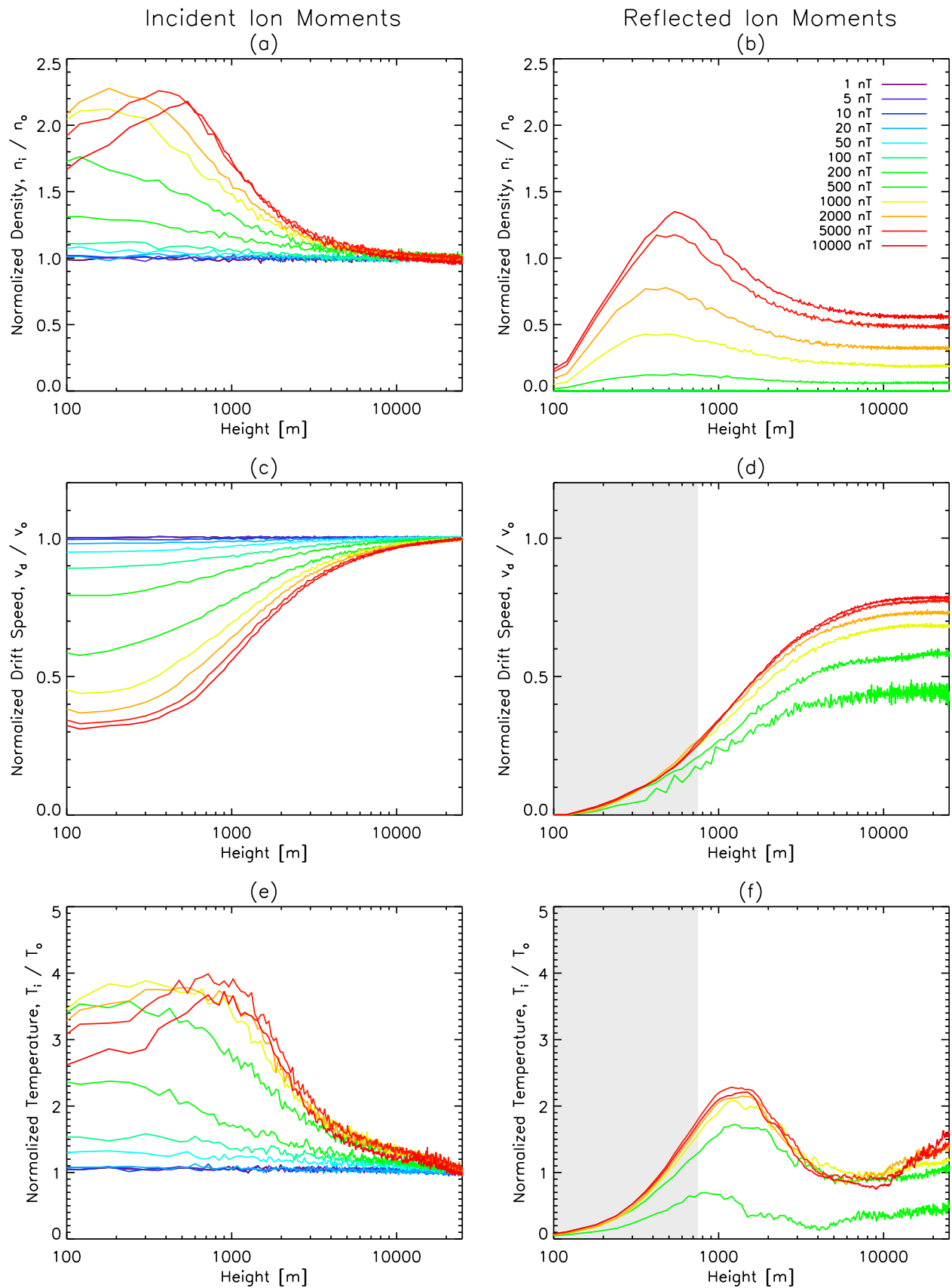
Figure 6. The normalized ion density, drift speed, and temperature for incident and reflected ions, respectively. For heights below 750 m, the incident and reflected populations cannot be separated into two populations. Thus, drift speeds and temperatures are shaded grey for reflected ions below this height.

slowed and reflected. The peak in density for both the incident and reflected protons occurs at heights of approximately 250 to 750 m just above the location of the peak electrostatic potential. Finally, for the strongest fields, the reflected proton density at heights far above the lunar surface reaches approximately 50% of the incident solar wind density. An increasing ion/electron mass ratio may be expected to correlate with a lower reflected proton density, as the corresponding electrostatic energies generated within the anomaly are somewhat smaller for larger ion/electron mass ratios (Figure 4).

[23] Figures 6c and 6d show the normalized solar wind proton drift speed as a function of height above the lunar surface for incident and reflected protons, respectively. The ability of the crustal fields to decelerate and effectively stagnate the solar wind via the generation of electrostatic potentials in a relatively short distance above the lunar surface is readily evident. For the incident beam, increasing field strengths progressively slow down the protons to a minimum of approximately 30% of the incident solar wind speed for the strongest crustal field strengths. For crustal field strengths greater than 100 nT, a reflected beam is accelerated away from the anomaly, reaching speeds from approximately 40% to 80% of the incident solar wind speed for fields ranging between 200 nT and 10,000 nT, respectively. Similar to the density, we also expect somewhat lower reflected bulk velocities for higher ion/electron mass ratios.

[24] Finally, Figures 6e and 6f show the temperature of the incident and reflected protons, respectively, as a function of height above the lunar surface for each crustal field strength. For the incident protons, low crustal field strengths (<20 nT) do not have an appreciable effect on the incident temperature, while fields stronger than this slowly increase the temperature as the beam approaches the surface. For the strongest field strengths, the temperature of the incident beam approaches four times that of the undisturbed case. For the reflected protons, the temperature generally increases as a function of crustal field strength, up to at maximum approximately twice the undisturbed value. We note that the reflected beam shows a somewhat variable temperature as a function of both height and field strength. For the smallest field strength with a reflected beam (200 nT) the variability is mainly due to low particle statistics in the reflected beam; however, for the larger field strengths, ion-ion two stream instabilities play a role in partially disrupting and heating both the reflected and incident beams. Further insight into the two-stream instability can be found upon inspection of the particle phase spaces and is discussed in the next paragraph. Other mechanisms, such as non-gyrotropic reflection or electromagnetic waves could plausibly heat the proton beams, similar to that observed by KAGUYA [Saito et al., 2012]; however, of these possible mechanisms, the $1\frac{1}{2}$-d PIC can only capture the two stream instability.

[25] Figure 7 shows a snapshot of the ion phase space (z versus $v_\parallel(z)$) for four crustal magnetic field strengths: (a) 5 nT, (b) 50 nT, (c) 500 nT, and (d) 5000 nT, after all simulations have come to equilibrium. For (a) 5 nT and (b) 50 nT, there is no ion reflection and all solar wind protons are incident upon the lunar surface. For (c) 500 nT, a small fraction of solar wind protons has been reflected by the self-consistent electrostatic potential shown in Figure 3a, while for (d) 5000nT, a significant fraction of solar wind protons are reflected by the correspondingly larger electrostatic

potential. In the high crustal field cases (c–d), the reflected stream of protons generates a collection of small-amplitude ion phase space holes that propagate toward and away from the lunar surface at velocities near the incident solar wind bulk velocity. These phase space holes are produced as a result of an ion-ion two-stream instability, which in turn contributes to the observed ion heating (cf. Figures 6e and 6f). The heating of ions from ion-ion two-stream instabilities has been predicted by previous theoretical and simulation analyses, and has been observed before in several different environments, including the lunar wake, the terrestrial auroral zone, the terrestrial plasma sheet boundary layer, and in laboratory experiments [Papadopoulos et al., 1971; Wahlund et al., 1992; Farrell et al., 1997, 1998]. Ion heating is more pronounced in the 5000 nT case, with phase space holes propagating both toward and away from the lunar surface. For low crustal field strengths with no proton reflection, no two stream instability is excited, and thus, no phase space holes are created. A preliminary stability analysis has suggested that while the positive slope in the ion distribution, df_i/dv, can lead to unstable wave growth, the instability can be somewhat offset by an increase in the electron temperature. Future will work address this instability in greater detail in order to understand the growth mechanisms of the two-stream instability and its effect on the ion distribution near the lunar surface.

[26] The flux of solar wind protons to the lunar surface can be readily calculated from the proton velocity distributions near the lunar surface, and is shown as a function of crustal magnetic field strength in Figure 8. For crustal field strengths of 200 nT or less, there is no solar wind shielding of the lunar surface by crustal anomalies within cusp regions. For crustal fields larger than 200 nT, the surface is partially shielded by the electrostatic potential, with the incoming proton flux dropping to approximately 50% for the largest crustal field strength of 10,000 nT. If typical values of maximum crustal field strength at the lunar surface are on the order of hundreds of nT (based on the Apollo 16 magnetometer and LP electron reflectometry measurements [Dyal et al., 1974; Halekas et al., 2001, 2010] and denoted in Figure 8 as a dashed line), then the estimated shielding of solar wind protons via electrostatic potentials in the cusp regions of lunar crustal fields is only on the order of 10%.

[27] In addition to the solar wind proton number flux, the solar wind proton energy flux can also be calculated, and is also shown as a function of crustal magnetic field strength in Figure 8. Similar to the proton number flux, the proton energy flux for weak crustal magnetic field cusps remains near unshielded solar wind values. For crustal fields greater than approximately 20 nT, the energy flux slowly decreases as a function of field strength reflecting the combined decrease in number flux and the deceleration of incident protons. For the strongest fields, the energy flux drops to approximately 25% of the unshielded solar wind; however, maximum measured lunar crustal field cusps would have proton energy fluxes on the order of 70% of the unshielded solar wind.

3. Discussion and Implications

[28] While the model presented here has considered a simplified interaction picture between the solar wind and the cusp regions of lunar crustal magnetic anomalies, we can
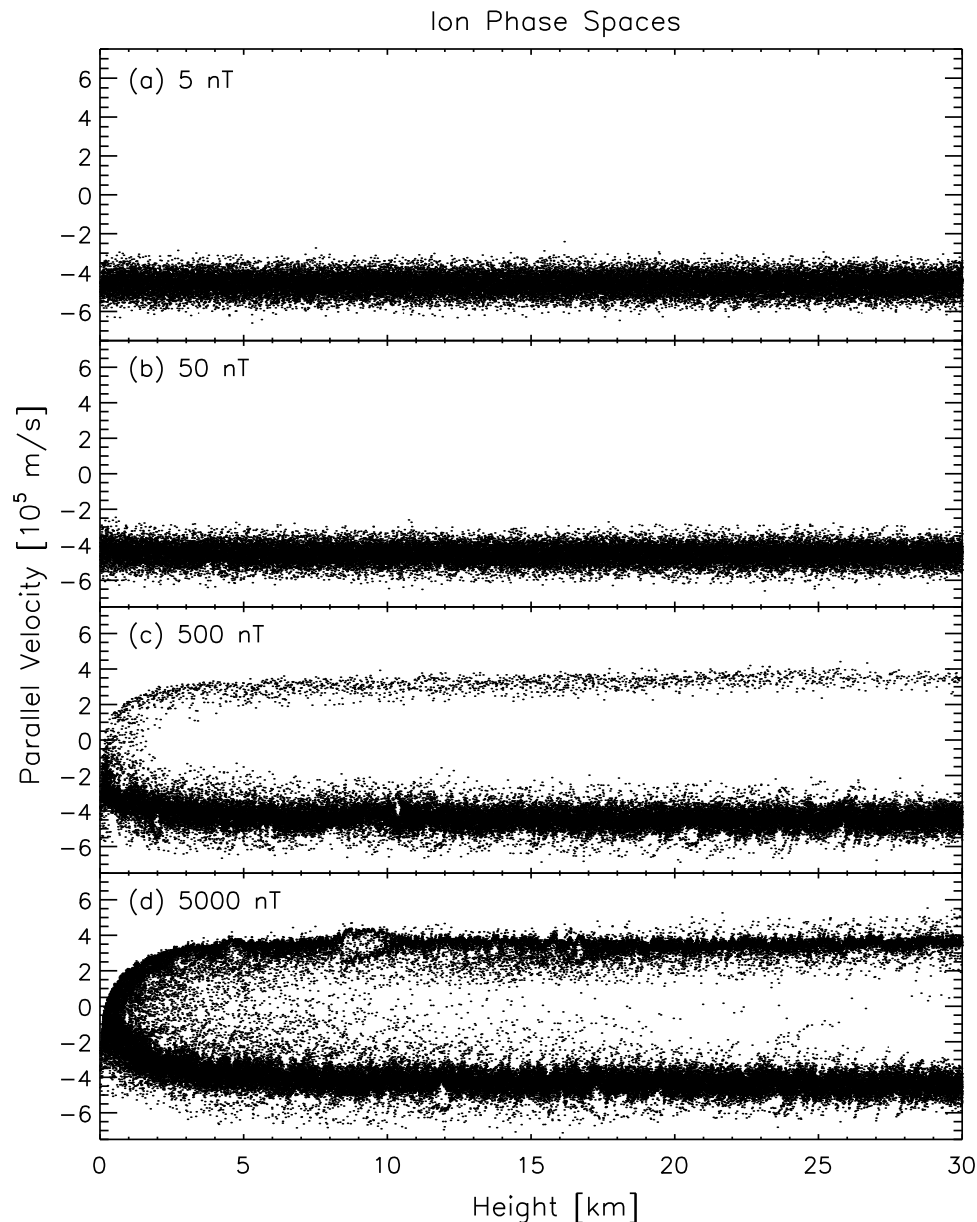
Figure 7. (a–d) The ion phase spaces (height above the lunar surface versus parallel velocity) for four different values of the crustal magnetic field strength at the lunar surface (5, 50, 500, 5000 nT, respectively).

draw several preliminary conclusions that, while limited by the geometry in this model, may have important analogues in the lunar case. We also present these conclusions with the goal of outlining future areas of investigation for higher dimensional PIC simulations, which can more accurately model this geometry.

[29] 1. In the absence of photoemission, a steady state, non-monotonic electrostatic potential builds up in front of the Moon within cusp regions of lunar crustal magnetic anomalies. The increasing potential from infinity acts to decelerate and for strong enough fields reflect a portion of the incoming supersonic solar wind protons, while accelerating solar wind electrons toward the Moon. This electric field, typically referred to as the 'ambipolar' field due to the charge separation induced by the presence of the crustal

magnetic field, is in fact partially due to the different pitch angle distributions of solar wind electrons and ions (as calculated analytically by [*Persson*, 1963, 1966]), and partially to the non-adiabatic interaction between the solar wind protons and the crustal magnetic fields. For heights less than approximately 150 m within crustal cusp regions, the near-surface plasma sheath, generated by the presence of the negatively charged lunar surface, causes the electrostatic potential to decrease from its maximum toward the surface. This region is dominated not by the crustal magnetic field interaction, but by the lunar surface electrostatic charge. Any solar wind protons energetic enough to overcome the ambipolar potential barrier within the cusp will be partially re-accelerated into the lunar surface, lessening any shielding effect of the crustal magnetic field cusp.
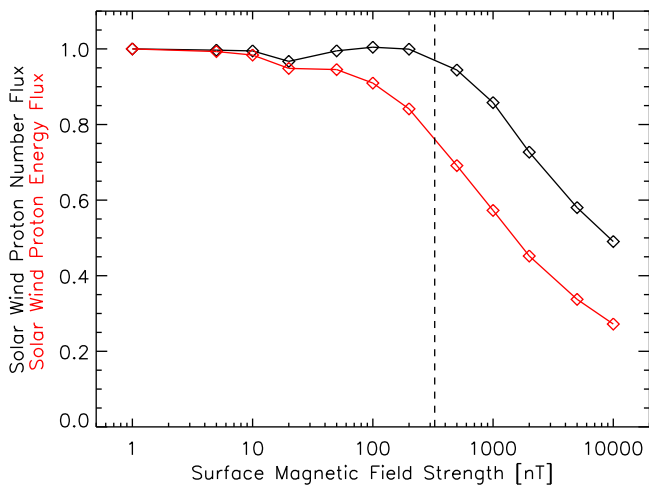
Figure 8. The normalized solar wind proton number flux (black) and solar wind proton energy flux (red) to the lunar surface as a function of crustal magnetic field strength at the surface. The dashed line represents the strongest measured crustal field strength at the lunar surface of 327 nT [*Dyal et al.*, 1974].

[30] As a preliminary check on the effect of photoemission from the lunar surface in the model, we have conducted runs at a subset of magnetic field strengths with photoelectrons emitted from the lunar surface with a current of $J_{ph} = 4.5 \ \mu A \ m^{-2}$ and a temperature of 2.2 eV, corresponding to laboratory measurements from lunar samples returned by the Apollo astronauts [*Feuerbacher et al.*, 1972]. While we do not present the full details of the simulations here, Figure 9 shows the ratio of the maximum electrostatic potential energy to the incident solar wind kinetic energy for a subset of crustal magnetic field strengths both with and without photoemission, similar to Figure 3b. The ratios show that the presence of photoemission does "short out" a small fraction of the potential by providing a source of electrons to counter the loss of solar wind electrons via magnetic reflection; however, the maximum ambipolar potentials are not significantly changed. In some sense, the surface photoelectron sheath is relatively de-coupled from the formation of large electrostatic potentials via ambipolar separation at much higher altitudes. Future work will address the near-surface lunar plasma environment within crustal magnetic fields in the presence of photoemission in more detail.

[31] 2. For electrostatic potentials within cusp regions strong enough to reflect incoming solar wind protons, an ion-ion two-stream instability is set up, leading to the production of ion phase space holes and associated ion heating in both the incident and reflected ion beams. This instability converts part of the solar wind proton bulk drift energy into thermal energy for the protons and is one possible explanation for the ion heating observed by KAGUYA [*Saito et al.*, 2012]. Additionally, we speculate that other heating mechanisms that the $1\frac{1}{2}$-d PIC code cannot address could also simultaneously exist, including a variety of electromagnetic waves and non-gyrotropic proton reflection, which would effectively broaden the reflected solar wind proton beam and appear as ion heating. While the electromagnetic waves would plausibly heat both the incident and reflected proton beams,

the non-gyrotropic reflection may act to heat only the reflected beam. Higher-dimensional PIC simulations may be able to investigate the possibility of non-gyrotropic reflection as an ion heating mechanism. Additionally, inclusion of electromagnetic effects with the aim of analyzing wave phenomena and interactions is also a worthy goal, but remains more distant.

[32] 3. The model qualitatively matches the recent KAGUYA spacecraft observations of the solar wind - lunar crustal magnetic field interaction at spacecraft altitudes, including the simultaneous presence of accelerated solar wind electrons and decelerated solar wind protons at spacecraft altitude implying a static, ambipolar electric field, a beam of solar wind protons reflected by the crustal magnetic anomaly below spacecraft altitude with less density and bulk speed than the incoming solar wind, and a solar wind proton heating region below spacecraft altitudes [*Saito et al.*, 2012].

[33] A comparison can be made by calculating the ratio of the KAGUYA-observed electrostatic potential drop to the incoming solar wind proton bulk energy, and comparing that with the PIC-predicted ratio shown in Figure 3b. We note that this comparison is an approximation since we do not specifically know the magnetic topology below KAGUYA during this observation; however, even such a first-order comparison is worthwhile. We first calculate extreme bounds on the net electrostatic potential drop observed by KAGUYA. For the minimum bound, KAGUYA measured an electrostatic potential of +150 V between the ambient solar wind and 25 km. Given an incoming solar wind proton bulk speed of 375 km/sec and in turn, a proton bulk energy of ≈730 eV [*Saito et al.*, 2012], the ratio of the minimum electrostatic energy to the incoming solar wind energy is 0.2. For an extreme upper bound, we can determine the electrostatic potential required to generate the reflected proton flux observed by KAGUYA of approximately $1.9 \times 10^{11} \ m^{-2} \ s^{-1}$, assuming no magnetic reflection whatsoever. Using a Maxwellian solar wind ion distribution with $kT_i = 10$ eV, this yields a net electrostatic potential (from infinity to its highest
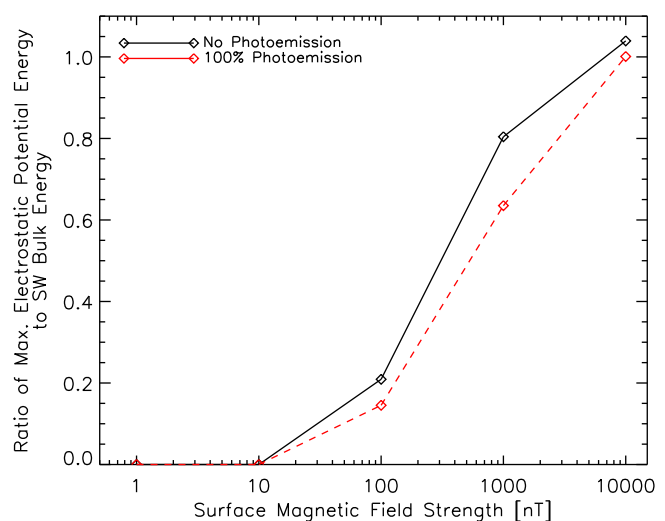

Figure 9. The ratio of the maximum electrostatic potential energy to the incident solar wind proton bulk energy as a function of crustal magnetic field strength both with (red) and without (black) photoemission from the surface.
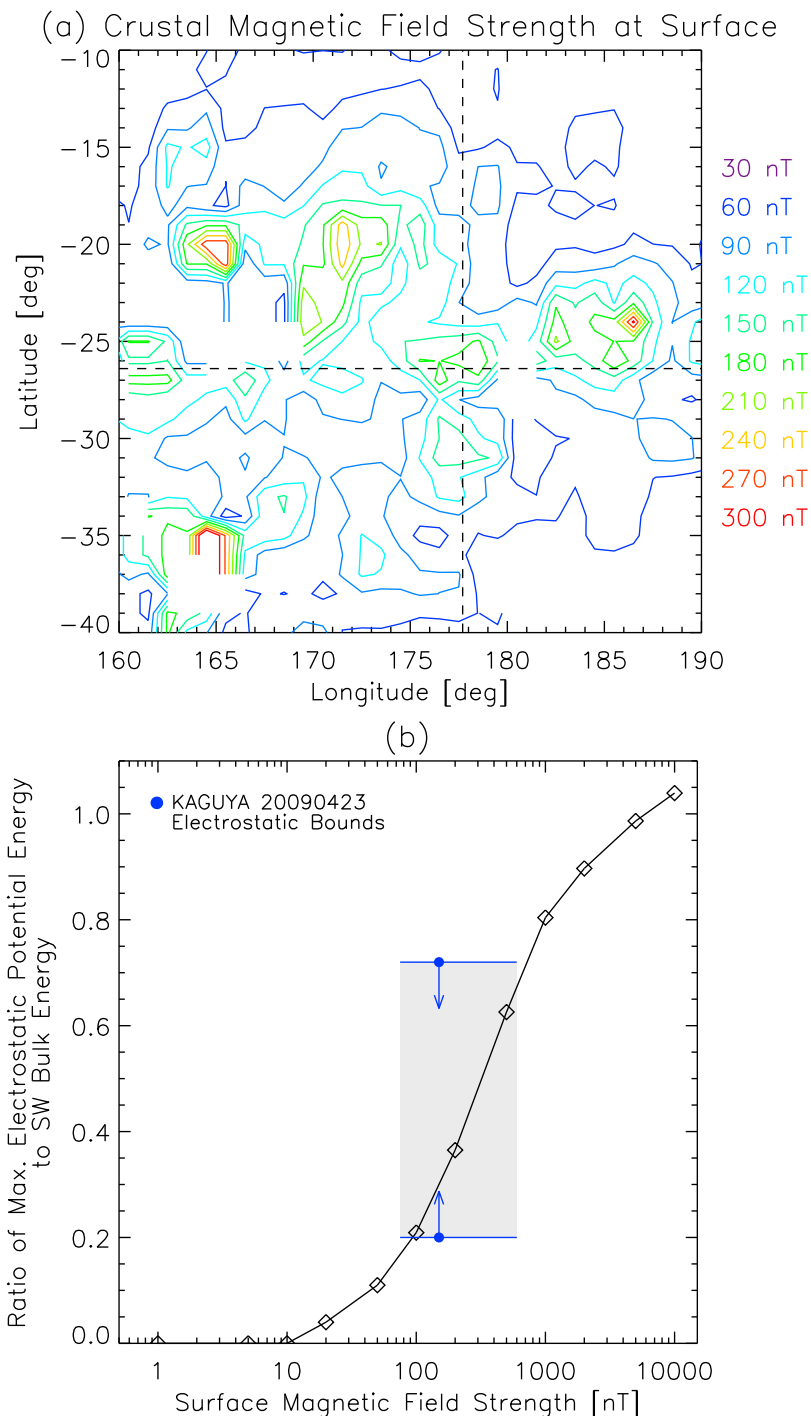
(a) Crustal Magnetic Field Strength at Surface

(b)

Figure 10. (a) A contour map of the crustal magnetic field strength at the lunar surface from the LP Electron Reflectometer model [*Mitchell et al.*, 2008]. The intersection of the crosshairs denotes the location of 20090423 KAGUYA measurement [*Saito et al.*, 2012]. (b) The ratio of maximum electrostatic potential energy to the incident solar wind proton bulk energy as a function of crustal magnetic field strength, similar to Figure 3b, but with the KAGUYA estimated minimum and maximum ratios and magnetic field strength from the 20090423 observation described in *Saito et al.* [2012] denoted in blue. The gray shaded region denotes the range of ratios and magnetic fields valid within error bars.

point) of approximately 530 V, or equivalently, a ratio of 0.72.

[34] Using the location of KAGUYA at this time, selenographic longitude 177.7° and latitude −26.4°, and the lunar crustal magnetic field model determined from the Lunar Prospector Electron Reflectometer instrument (shown in Figure 10a) [*Lin et al.*, 1998; *Mitchell et al.*, 2008], we can estimate the strength of the crustal field at the surface to be

approximately 150_{75}^{600} nT. Figure 10b shows the PIC-modeled ratio of maximum electrostatic potential to the incident solar wind bulk energy as a function of crustal field strength, identical to Figure 3b. Overplotted in blue on Figure 10b are the KAGUYA minimum and maximum estimated ratios at the corresponding surface crustal field strength. These bounds establish a range of ratios and magnetic field strengths consistent with the KAGUYA observations, denoted in Figure 10b by the gray shaded region. The PIC modeled ratio as a function of crustal field strengths falls directly within this range, providing a positive agreement between the model and the observation.

[35] 4. The cusp regions of crustal magnetic fields with magnitudes less than approximately 100 nT do not generate self-consistent electrostatic potentials capable of shielding from the solar wind from the surface, either in proton number flux or proton energy flux. The ability of the solar wind protons to penetrate all the way to the surface via cusp regions with little to no deceleration implies that cusp regions will experience a nearly equal rate of space weathering due to proton bombardment as areas of the lunar surface that do not possess crustal magnetic fields. As discussed in Section 1.2, observations of lunar swirls have noted the presence of small-scale, narrow regions within the swirl that appear as optically dark as regions outside of swirls [*Pinet et al.*, 2000]. These 'dark lanes' are hypothesized to be a result of the presence of cusp regions within crustal magnetic anomalies that allow the solar wind greater access to the surface than neighboring, magnetically shielded regions. The results from the simulations presented here support this hypothesis by quantifying that cusp regions require magnetic field strengths on the order of hundreds of nT in order to produce electrostatic potentials capable of shielding the lunar surface from solar wind protons, and even then, shield the surface only weakly. Given that the maximum strength of lunar crustal fields is on the order of hundreds of nT [*Mitchell et al.*, 2008], it is possible that nearly all crustal field cusp regions on the Moon are exposed to most, if not all, of the incoming solar wind proton flux. High-resolution measurements of crustal magnetic topology over swirl regions would be able to further strengthen the hypothesis for the formation of lunar swirl dark lanes if such measurements found a high degree of correlation between magnetic cusp regions and lunar swirl dark lanes [*Hemingway and Garrick-Bethell*, 2012]. Additionally, a more quantitative understanding of the relationship between crustal magnetic field strength and topology and the amount of space weathering on the lunar surface underneath such anomalies may help discriminate between the relative contributions of energetic solar wind proton bombardment, which is modified by the presence of crustal anomalies, and micrometeorite impacts, which are not affected by crustal anomalies, on the weathering of planetary surfaces exposed to space [*Pieters et al.*, 2000; *Hapke*, 2001; *Clark et al.*, 2002; *Loeffler et al.*, 2009].

[36] Surveys of lunar swirls have found that while all swirls are associated with crustal magnetic anomalies, the opposite is not true [*Kramer et al.*, 2011b], which would appear to be an argument against the solar wind shielding hypothesis. We suggest that these simulations may provide a reason why not all lunar magnetic anomalies possess a swirl on the surface below. If crustal field anomalies lacking a correlated swirl are oriented such that their primary magnetic topology is cusp-like, then our simulations predict that these anomalies, despite in some cases possessing magnitudes of hundreds of nT, will not shield the surface from the solar wind. In turn, the surface below these anomalies will suffer space weathering from proton bombardment at an equal rate to magnetically unshielded regions. This suggestion, along with recent studies indicating a high degree of correlation between magnetic field geometry and surface albedo [*Hemingway and Garrick-Bethell*, 2012], should be explored in order to further discern the viability of the solar wind shielding hypothesis for lunar swirl formation [*Hood and Schubert*, 1980; *Hood and Williams*, 1989].

4. Conclusion

[37] We have simulated the interaction between the solar wind and the cusps of lunar crustal magnetic anomalies with a self-consistent, electrostatic, $1\frac{1}{2}$-dimensional particle-in-cell code. These simulations were run for crustal magnetic fields of a dipolar nature, aligned such that the cusp of the dipole is along the simulation axis. The magnitude of the magnetic field at the lunar surface ranged from 1 nT to 10,000 nT in order to quantify the interaction as a function of field strength. Given the known complexity of lunar crustal magnetic fields, it is important to note that we see these simulations not as a final or all-encompassing description of the interaction of the solar wind with crustal magnetic fields, but rather as the first step in a series of increasingly sophisticated particle-in-cell models. We can easily identify many additional characteristics of this interaction that deserve study. This certainly includes the role that the magnetic topology plays in regulating the interaction. The simulations here have focused on cusp geometry, but of equal importance are crustal magnetic fields oriented such that they shield the surface. Understanding shielded magnetic geometries is especially critical for testing the viability of the solar wind shielding hypothesis for the formation of lunar swirls. Spacecraft observations and previous models have shown that lunar crustal magnetic fields can reflect solar wind protons with surprisingly high efficiency given their small scale and non-dipolar structure [*Harnett and Winglee*, 2003; *Lue et al.*, 2011]; however, the role that electrostatic fields play in governing the reflection of solar wind protons above magnetically shielded portions of the lunar surface is not yet well understood.

[38] Another important characteristic to study is the presence of higher order moments in the magnetic field. Crustal magnetic fields are highly non-dipolar and thus their magnitude will most likely have different altitude dependence than that simulated in this study. In turn, this should alter the electrostatic equilibrium and the solar wind proton number flux and energy flux to the lunar surface. Also, these simulations have shown that while crustal magnetic fields mainly govern the electrostatic interaction at altitudes greater than approximately 100 meters, they have also shown that the lunar surface, which charges in response to the presence of ambient plasma, plays a dominant role in governing the electrostatic and plasma environment for altitudes less than this. The lunar hemisphere exposed to the incident solar wind is also exposed to the presence of solar ultraviolet radiation, which will generate a photoelectron sheath above the lunar dayside [*Poppe and Horányi*, 2010]. Preliminary simulations have shown the photoelectrons from the lunar

surface serve to 'short out' some portion of the ambipolar electrostatic potential, although, not in significant enough amounts to fundamentally alter the production of large electrostatic potentials within magnetic cusp regions. We identify the investigation of the near-surface electrostatic environment within crustal magnetic anomalies as a next step given the known role that photoelectrons have in dominating the plasma environment near the lunar surface [*Poppe and Horányi*, 2010]. These simulations will allow us to evaluate a more recent theory of the formation of lunar swirls, in which the presence of magnetic anomalies above the lunar surface induces horizontal gradients in the electrostatic potential at the surface, and in turn, causes a net electrostatic transport of high-albedo, sub-micron sized lunar dust grains into magnetically shielded regions [*Garrick-Bethell et al.*, 2011].

[39] We also identify the simulation of the interaction of crustal magnetic fields with plasmas in the terrestrial magnetotail, which the Moon crosses each month for approximately five days, as an important subject of study. The Moon occasionally encounters the terrestrial plasma sheet, which, while not possessing the supersonic bulk flow of the solar wind, is nevertheless an energetic plasma with proton temperatures of approximately 1 to 10 keV [*Takahashi and Hones Jr.*, 1988; *Schriver et al.*, 1998]. The differences between the terrestrial plasma sheet and the solar wind offer an opportunity to compare and contrast the importance of various plasma characteristics in governing the interaction of crustal magnetic fields with ambient plasmas. A study of the terrestrial plasma sheet interaction with crustal fields and the lunar surface may also allow quantification of the rate of space weathering of the lunar surface near crustal anomalies while in the magnetotail.

[40] Our simulations may have implications for other airless bodies in the solar system that may possess crustal remanent magnetism, including asteroids, some of the moons of Mars and the outer planets, and Edgeworth-Kuiper Belt objects [*Hood*, 1995]. The asteroid 4 Vesta is known to have an unusually pristine surface [*Chapman*, 2004], which could be the result of solar wind shielding of its surface by remanent magnetic fields [*Vernazza et al.*, 2006; *Starukhina and McCord*, 2012]. The Dawn spacecraft, designed to explore 1 Ceres and 4 Vesta, may provide greater insight into the space weathering processes operating on these asteroids; however, the spacecraft does not include a magnetometer, and thus it remains an open question whether or not either object possesses an intrinsic magnetic field [*Russell et al.*, 2007]. Nevertheless, if Dawn finds evidence for differential space weathering of the Vestan surface, it may suggest magnetic surface shielding similar to that at the Moon.

[41] Finally, we have presented a comparison of this model with a single observation by the KAGUYA spacecraft of the interaction of the solar wind with crustal magnetic anomalies [*Saito et al.*, 2012] and found preliminary qualitative agreement. We plan to conduct a detailed comparison with spacecraft observations using data from the dual-probe ARTEMIS mission currently in orbit around the Moon [*Angelopoulos*, 2010; *Sibeck et al.*, 2011]. ARTEMIS is accumulating observations of both solar wind and terrestrial plasma sheet interactions with lunar crustal magnetic anomalies and presents a rich data set with which to compare to our model.

References

Angelopoulos, V. (2010), The ARTEMIS mission, *Space Sci. Rev.*, *165*, 3–25.

Bamford, R. A., et al. (2012), Minimagnetospheres above the lunar surface and the formation of lunar swirls, *Phys. Rev. Lett.*, *109*, 081101, doi:10.1103/PhysRevLett.109.081101.

Bell, J. F., and B. R. Hawke (1982), The Reiner Gamma Formation: Composition and origin as derived from remote sensing observations, *Proc. Lunar Planet Sci. Conf.*, *12*, 679–694.

Birdsall, C. K., and A. B. Langdon (1985), *Plasma Physics Via Computer Simulation*, McGraw-Hill, New York.

Blewett, D. T., B. R. Hawke, N. C. Richmond, and C. G. Hughes (2007), A magnetic anomaly associated with an albedo feature near Airy crater in the lunar nearside highlands, *Geophys. Res. Lett.*, *34*, L24206, doi:10.1029/2007GL031670.

Chapman, C. R. (2004), Space weathering of asteroid surfaces, *Annu. Rev. Earth Planet. Sci.*, *32*, 539–567.

Chen, F. F. (1984), *Introduction to Plasma Physics and Controlled Fusion*, Plenum, New York.

Clark, B. E., B. Hapke, C. Pieters, and D. Britt (2002), Asteroid space weathering and regolith evolution, in *Asteroids III*, pp. 585–599, Univ. of Ariz. Press, Tucson.

Clark, R. N. (2009), Detection of adsorbed water and hydroxyl on the Moon, *Science*, *326*, 562–564.

Dyal, P., C. W. Parkin, and C. P. Sonett (1970), Apollo 12 magnetometer: Measurement of a steady magnetic field on the surface of the Moon, *Science*, *169*(3947), 762–764.

Dyal, P., C. W. Parkin, and W. D. Daily (1974), Magnetism and the interior of the Moon, *Rev. Geophys.*, *12*(4), 568–591.

El-Baz, F. (1972), The Alhazen to Abul Wafa swirl belt: An extensive field of light-colored sinuous markings, *NASA Spec. Publ.*, *315*, 29–93.

Farrell, W. M., M. L. Kaiser, and J. T. Steinberg (1997), Electrostatic instability in the central lunar wake: A process for replenishing the void?, *Geophys. Res. Lett.*, *24*(9), 1135–1138.

Farrell, W. M., M. L. Kaiser, J. T. Steinberg, and S. D. Bale (1998), A simple simulation of a plasma void: Applications to Wind observations of the lunar wake, *J. Geophys. Res.*, *103*(10), 23,653–23,660.

Feuerbacher, B., M. Anderegg, B. Fitton, L. D. Laude, R. F. Willis, and R. J. L. Grard (1972), Photoemission from lunar surface fines and the lunar photoelectron sheath, *Proc. Lunar Sci. Conf.*, *3*, 2655–2663.

Freeman, J. W., and M. Ibrahim (1975), Lunar electric fields, surface potential and associated plasma sheaths, *Moon*, *14*, 103–114.

Fuller, M. (1974), Lunar magnetism, *Rev. Geophys.*, *12*(1), 23–70.

Garrick-Bethell, I., B. P. Weiss, D. L. Shuster, and J. Buz (2009), Early lunar magnetism, *Science*, *323*, 356–359.

Garrick-Bethell, I., J. W. Head III, and C. M. Pieters (2011), Spectral properties, magnetic fields, and dust transport at lunar swirls, *Icarus*, *212*, 480–492.

Halekas, J. S., D. L. Mitchell, R. P. Lin, S. Frey, L. L. Hood, M. H. Acuña, and A. B. Binder (2001), Mapping of crustal magnetic anomalies on the lunar near side by the Lunar Prospector electron reflectometer, *J. Geophys. Res.*, *106*(E11), 27,841–27,852.

Halekas, J. S., D. L. Mitchell, R. P. Lin, L. L. Hood, M. H. Acuña, and A. B. Binder (2002), Evidence for negative charging of the lunar surface in shadow, *Geophys. Res. Lett.*, *29*(10), 1435, doi:10.1029/2001GL014428.

Halekas, J. S., R. P. Lin, and D. L. Mitchell (2003), Magnetic fields of lunar multi-ring impact basins, *Meteorit. Planet. Sci.*, *38*(4), 565–578.

Halekas, J. S., R. P. Lin, and D. L. Mitchell (2005), Large negative lunar surface potentials in sunlight and shadow, *Geophys. Res. Lett.*, *32*, L09102, doi:10.1029/2005GL022627.

Halekas, J. S., D. A. Brain, D. L. Mitchell, and R. P. Lin (2006a), Whistler waves observed near lunar crustal magnetic sources, *Geophys. Res. Lett.*, *33*, L22104, doi:10.1029/2006GL027684.

Halekas, J. S., D. A. Brain, D. L. Mitchell, R. P. Lin, and L. Harrison (2006b), On the occurrence of magnetic enhancements caused by solar wind interaction with lunar crustal fields, *Geophys. Res. Lett.*, *33*, L08106, doi:10.1029/2006GL025931.

Halekas, J. S., D. A. Brain, R. P. Lin, and D. L. Mitchell (2008a), Solar wind interaction with lunar crustal magnetic anomalies, *Adv. Space Res.*, *41*, 1319–1324.

Halekas, J. S., G. T. Delory, D. A. Brain, R. P. Lin, and D. L. Mitchell (2008b), Density cavity observed over a strong lunar crustal magnetic

anomaly in the solar wind: A mini-magnetosphere?, *Adv. Space Res.*, *56*, 941–946.

Halekas, J. S., G. T. Delory, R. P. Lin, T. J. Stubbs, and W. M. Farrell (2008c), Lunar Prospector observations of the electrostatic potential of the lunar surface and its response to incident currents, *J. Geophys. Res.*, *113*, A09102, doi:10.1029/2008JA013194.

Halekas, J. S., R. J. Lillis, R. P. Lin, M. Manga, M. E. Purucker, and R. A. Carley (2010), How strong are lunar crustal magnetic fields at the surface?: Considerations from a reexamination of the electron reflectometry technique, *J. Geophys. Res.*, *115*, E03006, doi:10.1029/2009JE003516.

Halekas, J. S., A. Poppe, G. T. Delory, W. M. Farrell, and M. Horányi (2012), Solar wind electron interaction with the dayside lunar surface and crustal magnetic fields: Evidence for precursor effects, *Earth Planets Space*, *64*, 73–82.

Hapke, B. (2001), Space weathering from Mercury to the asteroid belt, *J. Geophys. Res.*, *106*(E5), 10,039–10,073.

Harnett, E. M., and R. Winglee (2000), Two-dimensional MHD simulation of the solar wind interaction with magnetic field anomalies on the surface of the Moon, *J. Geophys. Res.*, *105*(A11), 24,997–25,007.

Harnett, E. M., and R. M. Winglee (2002), 2.5D particle and MHD simulations of mini-magnetospheres at the Moon, *J. Geophys. Res.*, *107*(A12), 1421, doi:10.1029/2002JA009241.

Harnett, E. M., and R. M. Winglee (2003), 2.5-D fluid simulations of the solar wind interacting with multiple dipoles on the surface of the Moon, *J. Geophys. Res.*, *108*(A2), 1088, doi:10.1029/2002JA009617.

Hashimoto, K., et al. (2010), Electrostatic solitary waves associated with magnetic anomalies and wake boundary of the Moon observed by KAGUYA, *Geophys. Res. Lett.*, *37*, L19204, doi:10.1029/2010GL044529.

Hemingway, D., and I. Garrick-Bethell (2012), Insights into lunar swirl morphology and magnetic source geometry: Models for the Reiner Gamma and Airy anomalies, paper presented at 43rd Lunar and Planetary Science Conference, NASA, The Woodlands, Tex.

Hood, L. L. (1995), Frozen fields, *Earth Moon Planets*, *67*, 131–142.

Hood, L. L. (2011), Central magnetic anomalies of Nectarian-aged lunar impact basins: Probable evidence for an early core dynamo, *Icarus*, *211*, 1109–1128.

Hood, L. L., and N. A. Artemieva (2008), Antipodal effects of lunar basin-forming impacts: Initial 3D simulations and comparisons with observations, *Icarus*, *193*, 485–502.

Hood, L. L., and Z. Huang (1991), Formation of magnetic anomalies antipodal to lunar impact basins: Two-dimensional model calculations, *J. Geophys. Res.*, *96*(B6), 9837–9846.

Hood, L. L., and G. Schubert (1980), Lunar magnetic anomalies and surface optical properties, *Science*, *208*, 49–51.

Hood, L. L., and C. R. Williams (1989), The lunar swirls: Distribution and possible origins, *Proc. Lunar Sci. Conf.*, *19*, 99–113.

Hood, L. L., A. Zakharian, J. Halekas, D. L. Mitchell, R. P. Lin, M. H. Acuña, and A. B. Binder (2001), Initial mapping and interpretation of lunar crustal magnetic anomalies using Lunar Prospector magnetometer data, *J. Geophys. Res.*, *106*(E11), 27,825–27,839.

Kramer, G. Y., J.-P. Combe, E. M. Harnett, B. R. Hawke, S. K. Noble, D. T. Blewett, T. B. McCord, and T. A. Giguere (2011a), Characterization of lunar swirls at Mare Ingenii: A model for space weathering at magnetic anomalies, *J. Geophys. Res.*, *116*, E04008, doi:10.1029/2010JE003669.

Kramer, G. Y., et al. (2011b), M^3 spectral analysis of lunar swirls and the link between optical maturation and surface hydroxyl formation at magnetic anomalies, *J. Geophys. Res.*, *116*, E00G18, doi:10.1029/2010JE003729.

Kurata, M., H. Tsunakawa, Y. Saito, H. Shibuya, M. Matsushima, and H. Shimizu (2005), Mini-magnetosphere over the Reiner Gamma magnetic anomaly region on the Moon, *Geophys. Res. Lett.*, *32*, L24205, doi:10.1029/2005GL024097.

Lin, R. P., D. L. Mitchell, D. W. Curtis, K. A. Anderson, C. W. Carlson, J. McFadden, M. H. Acuña, L. L. Hood, and A. B. Binder (1998), Lunar surface magnetic fields and their interaction with the solar wind: Results from Lunar Prospector, *Science*, *281*, 1480–1484.

Loeffler, M. J., C. A. Dukes, and R. A. Baragiola (2009), Irradiation of olivine by 4 keV He$^+$: Simulation of space weathering by the solar wind, *J. Geophys. Res.*, *114*, E03003, doi:10.1029/2008JE003249.

Lue, C., Y. Futaana, S. Barabash, M. Wieser, M. Holmström, A. Bhardwaj, M. B. Dhanya, and P. Wurz (2011), Strong influence of lunar crustal fields on the solar wind flow, *Geophys. Res. Lett.*, *38*, L03202, doi:10.1029/2010GL046215.

Managadze, G. G., V. T. Cherepin, Y. G. Shkuratov, V. N. Kolesnik, and A. E. Chumikov (2011), Simulating OH/H$_2$O formation by solar wind at the lunar surface, *Icarus*, *215*, 449–451.

Mitchell, D. L., J. S. Halekas, R. P. Lin, S. Frey, L. L. Hood, M. H. Acuña, and A. Binder (2008), Global mapping of lunar crustal magnetic fields by Lunar Prospector, *Icarus*, *194*, 401–409.

Neish, C. D., D. T. Blewett, D. B. J. Bussey, S. J. Lawrence, M. Mechtley, B. J. Thomson, and The Mini-RF Team (2011), The surficial nature of lunar swirls as revealed by the Mini-RF instrument, *Icarus*, *215*, 186–196.

Noble, S. K., C. M. Pieters, and L. P. Keller (2007), An experimental approach to understanding the optical effects of space weathering, *Icarus*, *192*, 629–642.

Papadopoulos, K., R. C. Davidson, J. M. Dawson, I. Haber, D. A. Hammer, N. A. Krall, and R. Shanny (1971), Heating of counterstreaming ion beams in an external magnetic field, *Phys. Fluids*, *14*(4), 849–857.

Persson, H. (1963), Electric field along a magnetic line of force in a low-density plasma, *Phys. Fluids*, *6*(12), 1756–1759.

Persson, H. (1966), Electric field parallel to the magnetic field in a low-density plasma, *Phys. Fluids*, *9*(6), 1090–1098.

Pieters, C. M., E. M. Fischer, O. Rode, and A. Basu (1993), Optical effects of space weathering: The role of the finest fraction, *J. Geophys. Res.*, *98*(E11), 20,817–20,824.

Pieters, C. M., L. A. Taylor, S. K. Noble, L. P. Keller, B. Hapke, R. V. Morris, C. A. Allen, D. S. McKay, and S. Wentworth (2000), Space weathering on airless bodies: Resolving a mystery with lunar samples, *Meteorit. Planet. Sci.*, *35*, 1101–1107.

Pieters, C. M., et al. (2009), Character and spatial distribution of OH/H$_2$O on the surface of the Moon seen by M^3 on Chandrayaan-1, *Science*, *326*, 568–572.

Pinet, P. C., V. V. Shevchenko, S. D. Chevrel, Y. Daydou, and C. Rosemberg (2000), Local and regional lunar regolith characteristics at Reiner Gamma Formation: Optical and spectroscopic properties from Clementine and Earth-based data, *J. Geophys. Res.*, *105*(E4), 9457–9475.

Poppe, A., and M. Horányi (2010), Simulations of the photoelectron sheath and dust levitation on the lunar surface, *J. Geophys. Res.*, *115*, A08106, doi:10.1029/2010JA015286.

Poppe, A., J. S. Halekas, and M. Horányi (2011), Negative potentials above the day-side lunar surface in the terrestrial plasma sheet: evidence of non-monotonic potentials, *Geophys. Res. Lett.*, *38*, L02103, doi:10.1029/2010GL046119.

Poppe, A. R., J. S. Halekas, G. T. Delory, W. M. Farrell, V. Angelopoulos, J. P. McFadden, J. W. Bonnell, and R. E. Ergun (2012), A comparison of ARTEMIS observations and particle-in-cell modeling of the lunar photoelectron sheath in the terrestrial magnetotail, *Geophys. Res. Lett.*, *39*, L01102, doi:10.1029/2011GL050321.

Purucker, M. E. (2008), A global model of the internal magnetic field of the Moon based on Lunar Prospector magnetometer observations, *Icarus*, *197*, 19–23.

Purucker, M. E., and J. B. Nicholas (2010), Global spherical harmonic models of the internal magnetic field of the Moon based on sequential and coestimation approaches, *J. Geophys. Res.*, *115*, E12007, doi:10.1029/2010JE003650.

Richmond, N. C., and L. L. Hood (2008), A preliminary global map of the vector lunar crustal magnetic field based on Lunar Prospector magnetometer data, *J. Geophys. Res.*, *113*, E02010, doi:10.1029/2007JE002933.

Richmond, N. C., L. L. Hood, J. S. Halekas, D. L. Mitchell, R. P. Lin, M. Acuña, and A. B. Binder (2003), Correlation of a strong lunar magnetic anomaly with a high-albedo region of the Descartes mountains, *Geophys. Res. Lett.*, *30*(7), 1395, doi:10.1029/2003GL016938.

Russell, C. T., and B. R. Lichtenstein (1975), On the source of lunar limb compression, *J. Geophys. Res.*, *80*, 4700–4711.

Russell, C. T., P. J. Coleman Jr., B. R. Lichtenstein, G. Schubert, and L. R. Sharp (1973), Subsatellite measurements of the lunar magnetic field, *Proc. Lunar Sci. Conf.*, *3*, 2833–2845.

Russell, C. T., et al. (2007), Dawn mission to Vesta and Ceres: Symbiosis between terrestrial observations and robotic exploration, *Earth Moon Planet*, *101*, 65–91.

Saito, Y., et al. (2012), Simultaneous observation of the electron acceleration and ion deceleration over lunar magnetic anomalies, *Earth Planets Space*, *64*, 83–92.

Schriver, D., M. Ashour-Abdalla, and R. L. Richard (1998), On the origin of the ion-electron temperature difference in the plasma sheet, *J. Geophys. Res.*, *103*(A7), 14,879–14,895.

Schultz, P. H., and L. J. Srnka (1980), Cometary collisions on the Moon and Mercury, *Nature*, *284*, 22–26.

Sharp, L. R., P. J. Coleman Jr., B. R. Lichtenstein, C. T. Russell, and G. Schubert (1973), Orbital mapping of the lunar magnetic field, *Moon*, *7*, 322–341.

Sibeck, D. G., et al. (2011), ARTEMIS science objectives, *Space Sci. Rev.*, *165*, 59–91.

Starukhina, L. V., and T. B. McCord (2012), Asteroid shielding from solar wind: Calculation of the parameters of magnetospheres, paper presented at 43rd Lunar and Planetary Science Conference, NASA, the Woodlands, Tex.

Sunshine, J. M., T. L. Farnham, L. M. Feaga, O. Groussin, F. Merlin, R. E. Millikan, and M. F. A'Hearn (2009), Temporal and spatial variability of lunar hydration as observed by the Deep Impact spacecraft, *Science*, *326*, 565–568.

Takahashi, K., and E. W. Hones Jr. (1988), ISEE 1 and 2 observations of ion distributions at the plasma sheet-tail lobe boundary, *J. Geophys. Res.*, *93*, 8558–8582, doi:10.1029/JA093iA08p08558. .

Vernazza, P., R. Brunetto, G. Strazzulla, M. Fulchignoni, P. Rochette, N. Meyer-Vernet, and I. Zouganelis (2006), Asteroid colors: A novel tool for magnetic field detection? The case of Vesta, *Astron. Astrophys.*, *451*(3), L43–L46.

Wahlund, J.-E., F. R. E. Forme, H. J. Opgenoorth, and M. A. L. Persson (1992), Scattering of electromagnetic waves from a plasma: Enhanced ion acoustic fluctuations due to ion-ion two-stream instabilities, *Geophys. Res. Lett.*, *19*(19), 1919–1922.

Wang, X., M. Horányi, and S. Robertson (2012), Characteristics of a plasma sheath in a magnetic dipole field: Implications to the solar wind interaction with the lunar magnetic anomalies, *J. Geophys. Res.*, *117*, A06226, doi:10.1029/2012JA017635.

Whipple, E. C. (1981), Potentials of surfaces in space, *Rep. Prog. Phys.*, *44*, 1197, doi:10.1088/0034-4885/44/11/002.

Wieser, M., S. Barabash, Y. Futaana, M. Holmström, A. Bhardwaj, R. Sridharan, M. B. Dhanya, A. Schaufelberger, P. Wurz, and K. Asamura (2010), First observation of a mini-magnetosphere above a lunar magnetic anomaly using energetic neutral atoms, *Geophys. Res. Lett.*, *37*, L05103, doi:10.1029/2009GL041721.